Full Articles

Calculation of the adsorption—desorption hysteresis curves in narrow-pore systems

Yu. K. Tovbin, A. G. Petukhov, and D. V. Eremich*

L. Ya. Karpov Physicochemical Research Institute,
10 ul. Vorontsovo Pole, 105064 Moscow, Russian Federation.
Fax: +7 (495) 917 2490

The gas and liquid spinodal branches for an adsorbate located in narrow slit-shaped, cylindrical, and spherocylindrical pores were calculated. The adsorbate is modeled by Lennard-Jones spherical particles. The calculation was based on the lattice gas model taking into account the intermolecular interactions of nearest neighbors in the quasichemical approximation. The density—temperature diagrams for the gas and liquid spinodal branches in the pores are similar to the equilibrium vapor—liquid phase diagrams: they have a common critical point; the dense-phase branches are shifted to lower pore fillings, while the rarefied-phase branches are shifted toward higher pore fillings. The width of adsorption—desorption hysteresis loop in the adsorption isotherms for Lennard-Jones particles was analyzed as a function of the pore size and the interaction potential of the adsorbate with the pore walls. The effect of pore wall roughness and the accuracy of isotherm calculation on the width of the adsorption—desorption hysteresis loop in cylindrical pores is discussed

Key words: adsorption isotherm, hysteresis, phase diagrams, spinodal, slit-shaped pores, cylindrical pores, spherocylindrical pores, lattice gas model, quasichemical approximation.

Capillary condensation[1,2] is manifested in the adsorption and desorption isotherms as a reversible hysteresis loop. This is widely used in practice to determine the pore size distribution. A number of procedures for calculation of the experimental points on the adsorption and/or desorption branches of the hysteresis loop are used for this purpose.[1—5] Traditionally, theoretical description of the pore size distribution is based on the relationship between the equilibrium saturation vapor pressure in a pore and the characteristic pore size (the Kelvin equation).[2] However, in recent years, the adsorption—desorption hysteresis has been analyzed in terms of the concept according to which capillary condensation is considered as a first-order phase transition.[6] This approach involves the calculation of both branches of the adsorption—desorption hysteresis on adsorption isotherms, which increases the accuracy of calculation of the saturation vapor pressure in the pores with respect to that attained using the Kelvin equation. The pore size distribution function is determined predominantly from only the desorption branch.

Published in Russian in *Izvestiya Akademii Nauk. Seriya Khimicheskaya,* No. 5, pp. 813—823, May, 2007.

1066-5285/07/5605-0845

Analysis of the phase transformations in the pores allows simultaneous and independent comparison of both calculated branches of the hysteresis loop with experimental data, which increases the bulk of experimental data for the search of pore size distribution function.

To calculate the hysteresis loop, it is necessary to plot, under isothermal conditions, a spinodal curve, *i.e.*, a curve that separates the regions of stable and unstable states of the material with respect to minor perturbations. This plotting is usual for the bulk phase;[7] this is also used for adsorption systems. The points of the spinodal curve are special points of isotherms in which metastable regions switch to absolutely unstable states. These points correspond to the conditions $\partial(\ln P)/\partial\theta = 0$, where $\theta = 1/v$ is density (or average degree of filling of the system), v is the specific volume per molecule, and P is the bulk-phase pressure. The complete set of these points as a function of temperature defines the spinodal curve. The vapor spinodal branch corresponds to supercooled vapor, and the liquid branch corresponds to the superheated liquid.[7]

The physical reason for the existence of the adsorption spinodal branch is the fluctuation instability of the adsorption film against an increase in its thickness following the adsorbate condensation.[6] The desorption spinodal branch is due to the cooperative behavior of the fluid in the pore upon a decrease in the external pressure. The stability region of this branch is determined by the conditions of the onset of desorption at the end of the pore, *i.e.*, the temperature, the pore width, and the saturation vapor pressure at which the desorption starts. This pressure depends on the ratio of the interaction energy of the fluid molecules with the surface and with each other. The pressure in the desorption branch is believed[6] to almost coincide with the liquid—vapor equilibrium pressure in relatively long isolated pores. This is really the case provided that the contribution of the inhomogeneity of the substance states at the pore ends and inside the pore to the system behavior is low. Then the hysteresis loop is unambiguously determined by the adsorption spinodal branch and by the equilibrium density jump on the isotherm connecting the coexisting rarefied and dense phases. These calculations are carried out using Monte Carlo methods, integral equations, density functional theory, and lattice gas model.[8—13] No quantitative interpretation of the capillary condensation phenomenon exists as yet;[14] therefore, further development of the theory of this process is in progress.

This study uses the lattice gas model[15] to analyze the adsorption—desorption hysteresis in narrow-pore systems. At the molecular level, the lattice gas model takes into account the proper volume of molecules and the interaction between them. This approach allows one to model adsorption on active carbons, clays, and zeolites, and on globular and mesoporous adsorbents.

An analysis of phase diagrams carried out previously[16—18] has shown that in the case of narrow-pore adsorbents, full phase diagrams, *i.e.*, the diagrams covering the whole range of filling degrees of the porous system, are multidome. This is due to the fact that the spatial regions in which the adsorbate is separated into low- and high-density phases at a given external pressure in complex adsorption fields are determined by the nature of the adsorbate—adsorbent interaction potential.

We considered the effect of the width of isolated slit-shaped and cylindrical pores and the ratio of the adsorbate—adsorbent and adsorbate—adsorbate interaction energies on the hysteresis width in the adsorption isotherms. In complex heterogeneous systems, to which porous adsorbents belong, analysis of separate isotherms is difficult if no phase diagrams and their spinodal analogs are available. Previously, the diagrams of spinodal states or the effect of the molecular properties of narrow-pore adsorbent—adsorbate systems on the hysteresis width have not been studied.

Calculation procedures

Model. The local molecular equilibrium distributions of the adsorbate were calculated using the lattice gas model.[15] The description of the structure of the complex porous system was based on the procedure of identification of model regions of the porous system with a simple ideal geometry (supramolecular level) and implied the allowance for junctions (transition sections) of different regions of the system.[16] Slit-shaped, cylindrical, and other regular-shaped pores are chosen as system regions with an ideal geometry. The internal region of the adsorbent pore is described using the functions F_q and $F_{q,f}$; F_q is the normalized fraction of type q pores, $1 \le q \le N$, N is the number of pores with different sizes, $\Sigma_{q=1}^{N} F_q = 1$, $F_{q,f}$ is the normalized fraction of type f units for a pore of size q, $1 \le f \le t(q)$, $t(q)$ is the number of types of units in a pore of size q; $\Sigma_{f=1}^{t(q)} F_{q,f} = F_q$. The ways of construction of functions $F_{q,f}$ for slit-shaped, cylindrical, and spherocylindrical pores have been described previously.[16—19]

The pore volume of the system is split into separate elementary units $v_0 = \lambda^3$ (λ is the lattice constant with z nearest neighbors) corresponding to the size of the molecule, which rule out double occupancy of the unit with different molecules. The equations for the calculation of equilibrium characteristics of adsorption were constructed in the quasichemical approximation for inclusion of intermolecular interactions.[15] This approximation gives phase diagrams for pores of simple geometry, which are in good agreement with the diagrams obtained by molecular dynamics and Monte Carlo methods.[12,13,20,21] These equations have been repeatedly described in the literature[12,13,16—21] and we will not consider them here.

The local adsorption properties are characterized by local Henry constants $a_{q,f} = a_{q,f}^0 \exp(\beta Q_{q,f})$, where $a_{q,f}^0$ is the preexponential factor, $\beta = 1/(kT)$, $Q_{q,f}$ is the binding energy of the molecule with an adsorption center of type f in a pore of type q. The separation of the adsorbent into sections with an ideal structure with equal values $a_{q,f}$ and junction regions in

which the $a_{q,f}$ values vary from one pore cross-section to another allows one to consider a broad range of adsorbents. The equilibrium distribution of particles over units $\theta_{q,f}$ of different type is found from the solution of a set of nonlinear equations by the Newton iteration method with specified θ value. The accuracy of determination of local filling degrees of different type units $\theta_{q,f}$ was at least 0.1%. The equilibrium pressure of the adsorptive P was determined based on $\theta_{q,f}$ values.

Calculation of the $Q_{q,f}$ value. The interaction energy of a molecule with the surface will be represented as the integral taken over the solid space (Ω designates the integration region) at a specified atom—atom potential $U_{As}(\rho)$ for the adsorbate interaction with atoms of the solid:

$$Q_{q,f} = \int_{\Omega} U_{As}(\rho) n_s dV,\ U_{As}(\rho) = 4\varepsilon_{As}[(\sigma_{As}/\rho)^{12} - (\sigma_{As}/\rho)^6], \quad (1)$$

where ρ is the distance from unit f to element dV in the solid bulk, n_s is the distribution density of atoms of a solid in the adsorbent. The $Q_{q,f}$ value depends on the pore cross-section geometry and on the adsorbent material. We will consider the simplest geometrical models, namely, slit-shaped, cylindrical, and spherocylindrical pores.

A slit-shaped pore is assumed to be formed by two infinite solid plates parallel to the XZ plane. The Y axis is directed normal to the XZ plane. In an infinite slit-shaped pore, a group of units with identical properties forms monolayer k, then $F_k = 1/H$; here the subscript $q = 1$ is omitted and the number of monolayer is designated by k, H is the slit width in monolayers δ, $\delta = \lambda$ for $z = 6$ or $\delta = (2/3)^{1/2}\lambda$ for $z = 12$, here $\lambda = 2^{1/6}\sigma_{AA}$. For argon atoms, $\sigma_{ArAr} = 0.3405$ nm is the Lennard-Jones potential parameter.

The interaction potential of the adsorbate with the wall was calculated as the sum $U(y) + U(H-y)$, where $U(y)$ is the model potential (1) for the adsorbate—wall interaction, y is the distance to the nearest wall, $U(H-y)$ is the potential energy (1) for the adsorbate interaction with the second pore wall. The interaction of the adsorbate molecule with each of the walls was described by the potential (10—4),[22] summation over the graphite layers being performed up to the tenth layer inclusive. Traditionally, the combination rules are applied to the Lennard-Jones potential parameters $\sigma_{sA} = (\sigma_{AA} + \sigma_{ss})/2$ and $\varepsilon_{As} = (\varepsilon_{AA}\varepsilon_{ss})^{1/2}$ to relate the adsorbate—adsorbent interactions for individual components A and surface atoms s through the specified Lennard-Jones potential parameters.

For an infinitely long slit, the interaction energy of the molecule with the surface is represened by $Q_1 = \alpha\varepsilon$, $\varepsilon \equiv \varepsilon_{AA}$, where $\alpha = 9.24$ corresponds to the argon—carbon system,[17] $\alpha = 3.9$, to the argon adsorption on silica gel.[18] For $\alpha = 1.0$ or 0, the adsorbate attraction to the wall is either weak (as in polymer sorbents) or missing. For the second monolayer, $Q_2 = Q_1/8$, which corresponds to a decrease in the attraction in proportion to the cubed number of the layer counted off from the pore wall. For more remote layers with the number $f > 2$, it was assumed that $Q_{f>2} = 0$.[17] As a more accurate condition for the lack of influence of the wall on the molecules inside the pore, the relation $Q_f \leq 1/20\varepsilon$ was used.

In a cylindrical pore, splitting of the space into units and their grouping are based on the known value of the particle—wall interaction potential taking into account the symmetry of the inner space of the pore. Depending on the pore radius R_p, one (for $R_p = (h + 0.5)\delta$), four,[23] or six units (for $z = 6$ or 12, respectively, at $R_p = h\delta$) can be located at the center of a cylindrical pore. Here $h > 1$ is an integer value λ. The adsorption energy in cylindrical pores is calculated using a "delocalized" interaction potential of a particle (10—4) situated at distance y from the cylindrical wall of a pore with the radius R_p:[20,23]

$$U(y) = -2\pi\varepsilon_{As}n_s\sigma_{As}^2\left\{\sum_{j=0}^{\infty}\left(\frac{\sigma_{As}}{R_p + j\Delta - y}\right)^4 f^{(4)}\left(\frac{y}{R_p + j\Delta}\right) - \right.$$

$$\left. - \frac{2}{5}\left(\frac{\sigma_{As}}{R_p - y}\right)^{10} f^{(10)}\left(\frac{y}{R_p}\right)\right\}, \quad (2)$$

where n_s is the density of atoms of a solid, Δ is the distance between the layers of atoms in the solid, ε_{As} and σ_{As} are Lennard-Jones interaction potential parameters for atoms A and s. The dependence of the interaction potential of the adsorbate with curved smoothened layers of atoms of the solid *vs.* distance is described by means of polynomial coefficients of the polynomial function $f^{(m)}(x) = \sum_{k=0}^{10} a_{mk}x^k$, which are presented in Table 1. Here the argument of the function $x = y/(R_p + j\Delta)$, where j is the number of the layer of solid atoms. The index $m = 4$ corresponds to the attractive branch of the potential, while $m = 10$ corresponds to the repulsive branch.

With $R_p \to \infty$ and with retention of the distance between the adsorbate and the pore wall, potential (2) is transformed into the potential for a flat wall.[22] For example, for the graphite basis face, the surface density of the carbon atoms $n_s = 38.6$ atom nm^{-2}, and the distance between the graphite layers $\Delta = 0.335$ nm.

For curved surfaces inside cylindrical and spherical pores, the Q_1 values depend on the curvature: the smaller the radius, the greater Q_1. For units in the second monolayer, the equality $Q_2 = Q_1/(8—10)$ is retained above the curved surfaces, which corresponds to a decrease in the attraction in proportion to the number of the layer cubed (f^3, where f is the monolayer number counted off from the pore wall); in addition, $Q_{f>2} = 0$. The diameters of cylindrical and spherical regions are expressed through the linear size of the unit λ.

The regular structure of spherocylinders will be designated by $D_s—D_c—L_c$, where D_s is the sphere diameter, D_c is the cylinder diameter, L_c is the length of the cylindrical channel.[19] The units of pores with equal energies $U(y)$ (2) refer to the same type. The internal units removed from the pore walls to distances

Table 1. Coefficients a_{mk} of the function $f^{(m)}(x)$[21,23]

k	a_{4k}	a_{10k}
0	4.71239	7.73126
1	−18.84855	−77.08463
2	57.64824	563.1619
3	−134.9114	−2820.991
4	253.9246	9608.343
5	−378.7086	−21794.03
6	420.1712	32000.29
7	316.4436	−28996.07
8	141.4307	14672.09
9	−27.97551	−3162.542

where the bond energies $Q_f(1)$ are about $\varepsilon/20$ or lower were classified as the central units of the pore.

Calculation conditions. The lattice with the number of nearest neighbors $z = 6$ will be used as the key lattice structure, as it has been repeatedly noted that this structure provides the best agreement of the critical parameters with experimental data for bulk fluids;[15] the lattice with $z = 12$, which corresponds to the closest packing of spherical molecules, will also be used. For qualitative analysis of spinodal diagrams and the effect of the molecular properties of the system on the width of the hysteresis loop, we will consider only the nearest neighbors. The energy of lateral interactions between the adsorbate molecules was determined using the Lennard-Jones potential $\varepsilon(r) = U_{AA}(r) = 4\varepsilon_{AA}[(\sigma_{AA}/r)^{12} - (\sigma_{AA}/r)^6]$, $r/\lambda = 1$ corresponds to the potential minimum.

A typical feature of the liquid—vapor separation curve for narrow-pore systems is the fact that a considerable fraction of the pore volume is concentrated in several near-surface layers having their own domes in the diagram.[16—19] The densities of the coexisting gas and liquid phases were found using the Maxwell plotting in the dimensionless coordinates θ—$\ln(a_0P)$.[15] Here P is the external pressure of the thermostat vapor (outside the pore) usually measured under experimental conditions. The appication of the Maxwell rule to porous systems does not differ from that for the bulk phase. The only exception is the adsorbate density range involved in the capillary condensation. This range corresponds to filling of a part of the pore volume rather than the whole system volume as in the bulk phase.[16—24]

The pressure in a pore that is sufficiently large for the wall potential to have no influence on the capillary condensation conditions is considered as the bulk pressure (for argon, this characteristic pore size exceeds 15 nm). The secant lines connect the densities of coexisting vapor and liquid phases on different isotherm branches. On the basis of special points of the isotherms for which the derivatives $\partial(\ln P)/\partial\theta = 0$, the points that refer to the gas and liquid spinodal branches are determined.

In the bulk phase (or for very large pores), the critical temperature $(\beta_b\varepsilon)^{-1} = 1.234$ for the lattice with $z = 6$ and 0.408 for $z = 12$. The phase diagrams were constructed in the reduced temperature $\tau = T/T_c(b)$ and dimensionless density θ, where T is the current temperature, $T_c(b)$ is the critical temperature in a very large pore where the effect of the walls can be neglected.

For the sake of simplicity, it was taken that $a_{q,f}{}^0 = a_0$. The dimensionality of a_0 is usually proportional to the pressure dimensionality. Then the local Henry constants $a_{q,f} = a_0\exp(\beta Q_{q,f})$, which allows one to take into account only the relative influence of the wall potential $Q_{f,q}$ with respect to the bulk phase. Below all pressures are given in the dimensionless units of the product a_0P, where $a_0 = 1$. Thus it becomes possible to analyze arbitrary relative characteristics of adsorption without attributing them to particular properties of the adsorbate and the adsorbent. The difference between the densities of coexisting vapor and liquid is the density jump determined by the Maxwell rule at the given temperature T. For the bulk phase, this density jump corresponds to the dimensionless saturation vapor pressure P_0.

Results and Discussion

The adsorption isotherms in a very large pore for three temperatures, namely, below the critical temperature (curve *1*), at the critical temperature (curve *2*), and above the critical temperature (curve *3*), are shown in Fig. 1, *a*. Below the critical temperature the adsorbate is separated into dense and rarefied phases. The density jump *BDF* on the isotherm during adsorbate condensation is shown by continuous line. The points on curve *1* designate the nonequilibrium (or metastable) section of isotherm *BCDEF*, which has the traditional shape of a van der Waals loop.[7,15,22] The areas of regions *DEF* and *DBC* constructed according to the Maxwell rule are equal; the densities in points *B* and *F* correspond to the equilibrium densities of the coexisting gas and liquid phases. The dashed line *AE* corresponds to the density jump on passing from the liquid-phase spinodal *EF* to the vapor phase, and the dashed line *CG* corresponds to the density jump on passing from the gas spinodal *BC* to the liquid phase. The pressure difference in points *F* and *E* determines the width of the metastable liquid-phase region, while the pressure difference in points *C* and *B* shows the width of the metastable vapor-phase region.

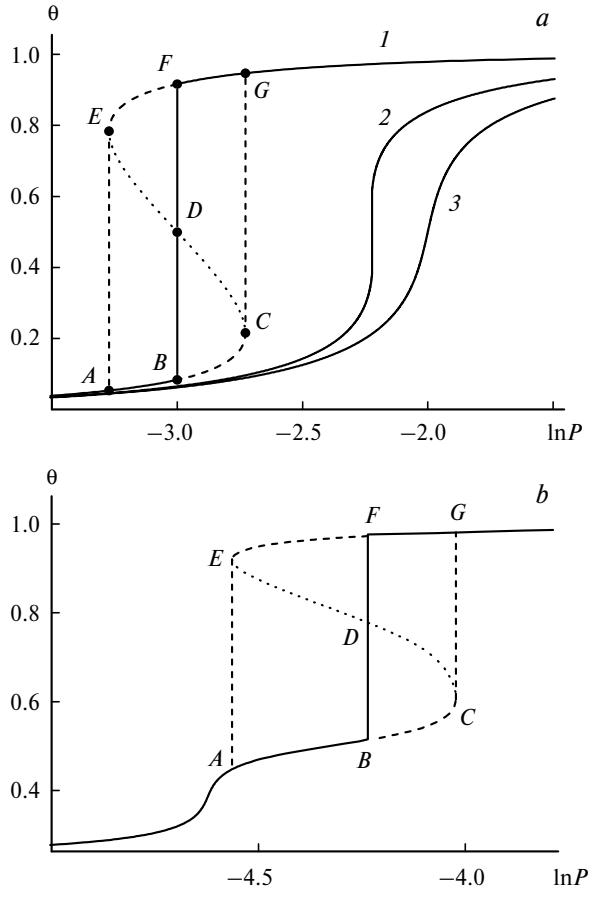

Fig. 1. *a*. Argon adsorption isotherms for $\tau = 0.73$ (*1*), 1.0 (*2*), and 1.1 (*3*) in a large pore ($z = 12$); *b*. Argon adsorption isotherm in a slit-shaped carbon pore with $H = 8$ monolayers ($z = 6$) with a loop corresponding to the formation of a third dome in the phase diagram (see below) at $\tau = 0.67$.

Analogous adsorption isotherm for an infinite slit-shaped pore eight monolayers wide is shown in Fig. 1, *b*. In narrow pores, the critical temperature $T_c(H)$ for slits or $T_c(D)$ for cylinders depends on the characteristic size of the pore. As the characteristic size H or D decreases, the critical temperature drops.[24—30]

Curves *ABDFG* (Fig. 1) form the equilibrium isotherm. The loop related to the central part of the pore is designated by letters in Fig. 1, *b*.

Three analogous secant lines (*AE*, *BF*, *CG*) can be plotted for all spatial regions within the pore bulk in which liquid—vapor phase separation takes place at different temperatures. The initial and final densities of each secant line depend only on the temperature. The sets of initial and final densities at temperatures $T < T_c$ for these three secant lines represent the coexistence curve of the vapor and liquid phases in a very large pore (Fig. 2, *a*), *i.e.*, the phase diagram of the sample (curve *1*) and analogous diagrams for the vapor (curve *3*) and liquid (curve *2*) spinodal branches.

Figures 2, *b*, *c* also show the equilibrium phase diagrams (curves *1*) and spinodal diagrams (curves *2* and *3*) for the adsorbate occurring below the critical temperature for the given pores $T \le T_c(H,D)$ in a slit-shaped pore with a width of seven monolayers ($z = 6$) and in a cylindrical pore with a diameter of 15 monolayers ($z = 12$).

Figure 2, *a* shows only one dome, as the contributions of the near-surface layers are minor. In Fig. 2, *b*, domes *I* and *II* refer to adsorbate separation into layers near the surface in the first and second monolayers. For these, the critical temperatures are considerably lower than for the third dome. Figure 2, *c* also presents two near-surface domes; the second dome distorts essentially the shape of the spinodal dome for the central particle of the pore. Figure 2, *d* demonstrates the difference between the patterns of spinodal secant lines for different temperatures. The difference of the structure type of the spinodal diagram for a cylindrical pore from that for a slit-shaped pore (see Fig. 2, *b*) is related to the predominant contribution of near-surface regions, the lattice type structure z, and a lower temperature. Thus, the pattern of the spinodal diagrams depends on all molecular properties of the adsorbate—adsorbent system.

The equilibrium state diagrams and spinodal branches in the spherocylindrical system $D_s—D_c—L_c = 20—15—15$ ($z = 6$) composed of alternating sections of cylindrical

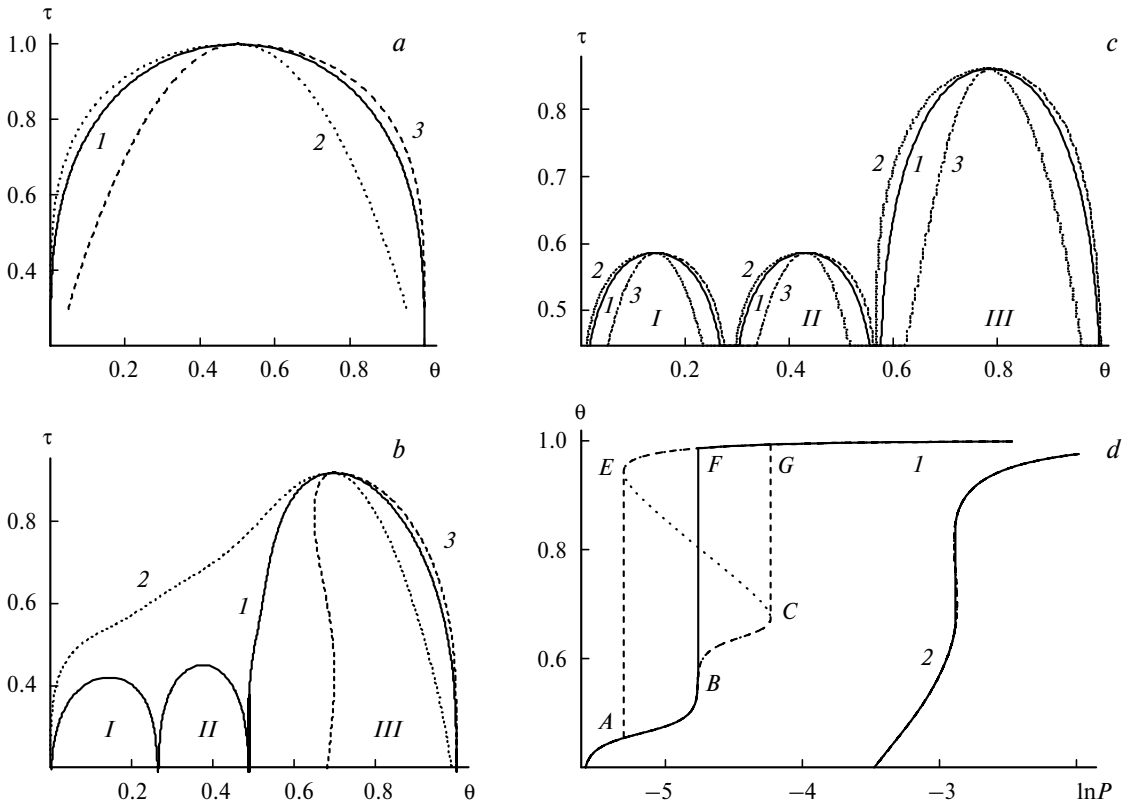

Fig. 2. *a*. Phase diagrams of the equilibrium state and spinodal branches in the bulk phase ($z = 12$); *b*. Phase diagram for argon in a carbon slit-shaped pore with $H = 7$ monolayers and its analogs for vapor and liquid spinodal branches ($z = 6$); *c*. Phase diagram for argon in a cylindrical pore with $D = 15\delta$, $z = 12$. Curves *1*, *2*, and *3* correspond to the equilibrium phase diagram, desorption and adsorption spinodal diagrams; *I*—*III* are dome numbers; *d*. Adsorption isotherms for a cylindrical pore with metastable sections ($z = 12$) for two temperatures: $\tau = 0.82$ (*1*) and 0.55 (2).

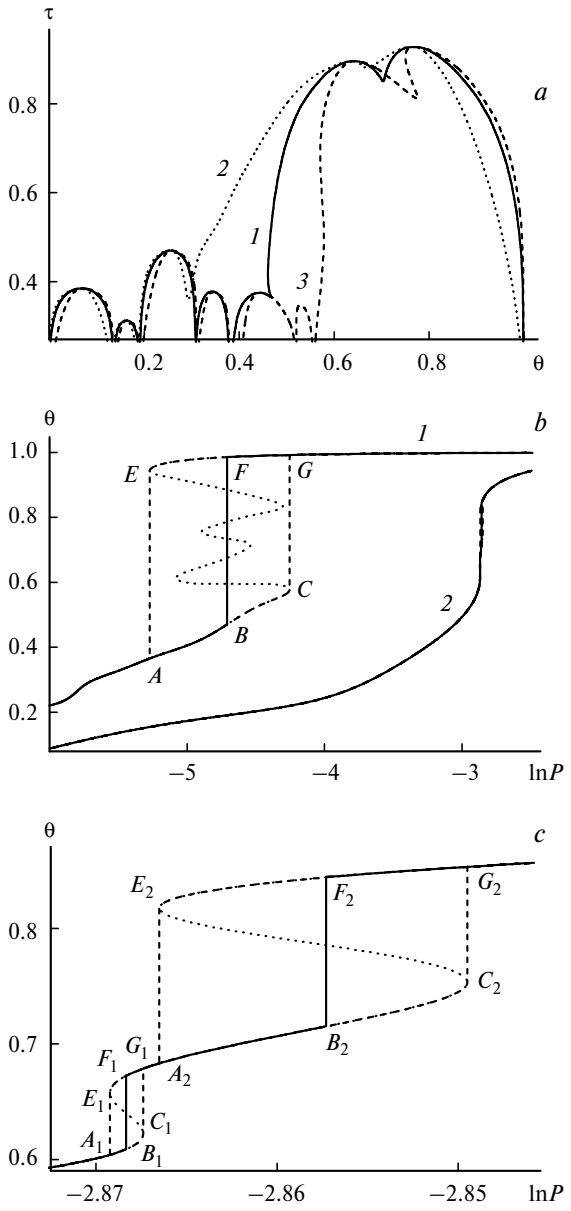

Fig. 3. *a*. Phase diagrams of the equilibrium state and spinodal branches in a spherocylindrical system with D_s—D_c—L_c = 20—15—15 (z = 6); *b*. Adsorption isotherms at temperatures $\tau = 0.89$ (*1*) and 0.49 (*2*); *c*. A section of the adsorption isotherm at $\tau = 0.89$.

pores and truncated spherical pores are shown in Fig. 3, *a*. This is a more complex porous system, and the phase diagram is more sophisticated. The near-surface domes are seen to split into six smaller domes, while the central dome, into two ones. Hence, the spinodal diagrams also become more complicated. The full adsorption isotherms for two temperatures are presented in Fig. 3, *b*. Curve *2* for low temperature illustrates how the units of different types are combined into a single dome on the equilibrium and spinodal diagrams.

Due to different magnitudes of pressure changes on the *x*-axis in Fig. 3, *b*, all features of the isotherms over a broad temperature range cannot be depicted on the same scale; therefore, Fig. 3, *c* shows a section of curve *1* for Fig. 3, *b* at a high (near-critical) temperature. It can be seen from Fig. 3, *a* that at high temperature, both equilibrium and spinodal diagrams exhibit two domes. These domes correspond to the capillary condensation conditions for the central units at the mouth (left dome) and at the center of the spherical part (right dome). In Fig. 3, *c*, coexisting densities B_1F_1 correspond to the left dome in the equilibrium phase diagram, while the coexisting densities B_2F_2 correspond to the right dome. The secant lines A_1E_1 and A_2E_2 correspond to two domes in curve *2* and secant lines C_1G_1 and C_2G_2 correspond to two domes in curve *3* (see Fig. 3, *a*).

Thus, in all situations (see Figs 2 and 3), both spinodal branches generate spinodal diagrams at different temperatures that represent analogs of phase diagrams for the corresponding pairs of low- and high-density filling degrees. For the vapor (adsorption) branch, the corresponding high-density filling degree at points *G* occurs in the liquid region of the isotherm (see Figs 2 and 3, curves *3*). For the liquid (desorption) branch, the corresponding low-density filling degree at points *A* is located in the vapor section of the isotherm (see Figs 2 and 3, curves *2*).

In the general case, the pattern of density—temperature spinodal diagrams for the gas and liquid spinodal branches in the pores is similar (but not identical) to the equilibrium vapor—liquid phase diagrams: they have a common critical point and their dense-phase branches are shifted to lower pore fillings, while the rarefied-phase branch is shifted to higher fillings.

The critical temperatures for the near-surface phase transitions are much lower than for the central pore region. Therefore, these temperatures are normally not reached in the experiments in analysis of adsorption isotherms for nitrogen, argon, and some other gases used in practice for finding the pore size distribution function based on the adsorption hysteresis data. In what follows we describe the hysteresis loop considering only those regions of isotherms that refer to so-called volume filling of the central part of the pore. This loop is observed at pressures exceeding the pressure of adsorbate film formation on the pore walls. The capillary condensation process is determined by filling of the central regions of the pores; therefore, the properties of hysteresis loops for near-surface monolayers are not considered below.

It follows from the general structure of phase diagrams[16–19] that in the case of more complex pores, it may happen that the numbers of domes in the equilibrium and spinodal phase diagrams would be unequal (see also Fig. 3, *a*). This is due to combination of two or several "equilibrium loops" into one, whereas the adsorption branch has two or more density jumps. As a rule, the

desorption branch has a smaller number of domes, while the adsorption branch contains a larger number of domes than the equilibrium phase diagram.

There is one more feature of isothermal measurements of adsorption isotherms under equilibrium conditions. According to the existing views on the physical nature of the adsorption—desorption hysteresis, a strictly equilibrium distribution of adsorbate molecules exists during desorption. Therefore, when analyzing the hysteresis width, one should consider only the difference between pressures on the adsorption spinodal (points *C*) and the equilibrium value P_0 (points *B*): $\Delta P = P_a(H,D) - P_0$, where $P_a(H,D)$ is the spinodal gas branch pressure in a slit-shaped pore of width H or a cylindrical pore of diameter D. Both the $P_a(H,D)$ value and the saturation vapor pressure P_0, as well as their ratio $\Delta P/P_0$ are functions of temperature. For the bulk phase, the width of the hysteresis loop was designated by $\Delta P_{bulk} = P_a(H,D\to\infty) - P_0$.

The temperature dependences of the saturation vapor pressure P_0 for a large pore (*1* and *2*) and the hysteresis width (ΔP) for a large (*3*) and cylindrical pore with D = 14 monolayers (*4*) are presented in Fig. 4, *a*. The dependences of the width of the hysteresis loop for a large pore and different lattice structures with z = 6 (*1*) and 12 (*2*), normalized to $P_0(T)$, are shown in Fig. 4, *b*. A similar dependence of the hysteresis width in a cylindrical pore with D = 14 monolayers for different lattice structures with z = 6 (*1*) and 12 (*2*) normalized to the loop width for a very large pore, $\Delta P_{bulk}(T)$, is presented in Fig. 4, *c*.

All of the temperature dependences of the loop width $\Delta P(T)$ have a maximum. This is due to the fact that both at $T \to 0$ and at $T \to T_c(H,D)$, the hysteresis loop disappears, $\Delta P(T) = 0$. The position of the maximum depends on the molecular properties of the adsorbate—adsorbent system. For curve *1* (z = 6, see Fig. 4, *b*), the maximum of

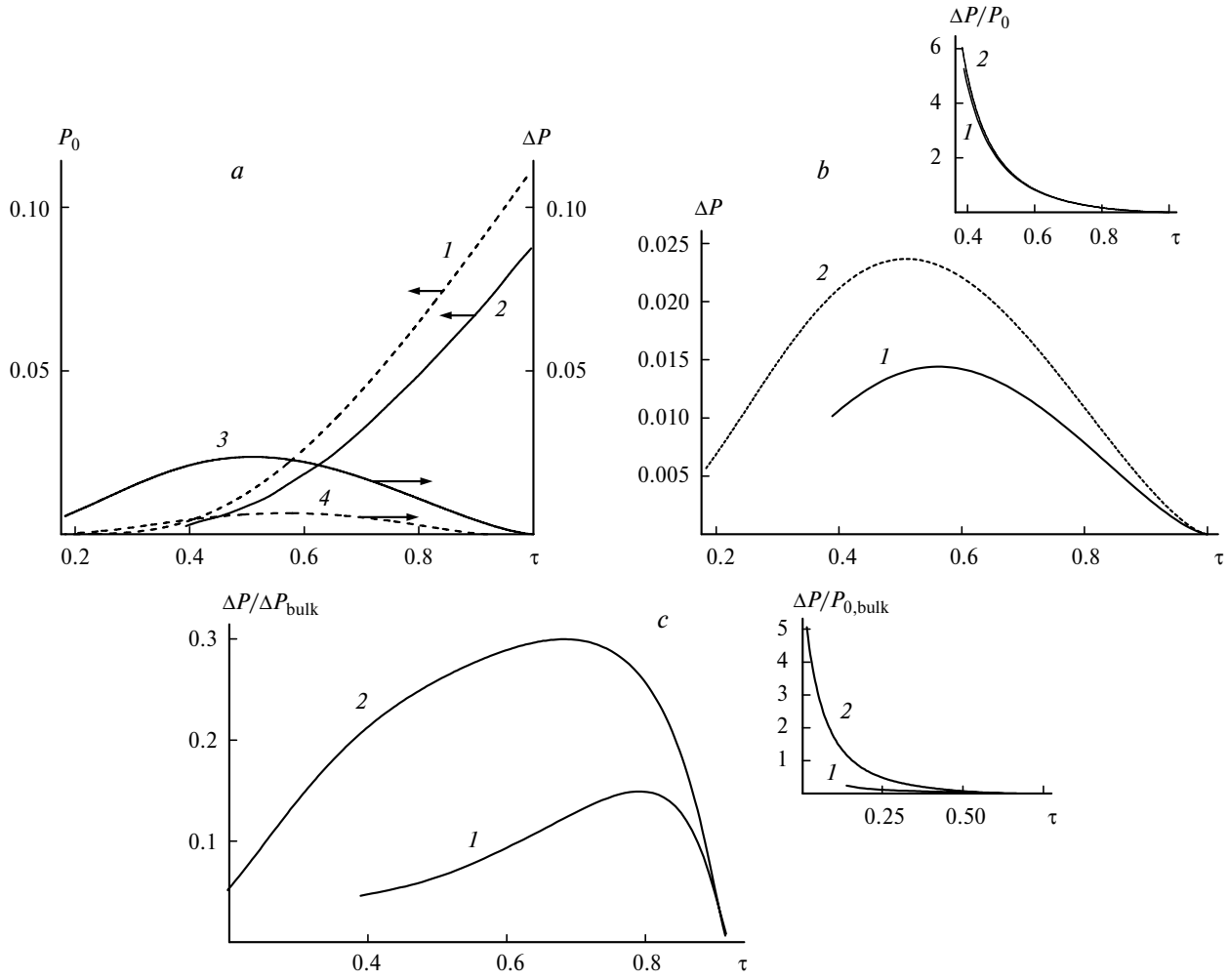

Fig. 4. *a*. Temperature dependences of the saturation vapor pressure for a large pore with z = 12 (*1*) and 6 (*2*) and of hysteresis width for a large (*3*) and cylindrical pore with D = 14 monolayers (*4*) for z = 12; *b*. Hysteresis width in a large pore for different lattice structures with z = 6 (*1*) and 12 (*2*), the inset shows the normalized $\Delta P(T)/P_0(T)$ ratios; *c*. Hysteresis loop in a pore with D = 14 monolayers for different lattice structures with z = 6 (*1*) and 12 (*2*), the inset shows the normalized $\Delta P(T)/P_0(T)$ ratios.

$\Delta P(T)$ refers to $\tau = 0.56$ (the maximum value $\Delta P(T) = 0.0144$), while for curve *2* ($z = 12$), the maximum refers to $\tau = 0.51$ ($\Delta P(T) = 0.0237$). Hence, in the critical points, the values $P_0 = 0.088$ ($z = 6$) and $P_0 = 0.112$ ($z = 12$). For Fig. 4, *c*, the loop width is normalized to the corresponding width of the hysteresis loop in a large pore (bulk phase). The possibility of this normalization is due to the fact that the critical temperature in the pore is lower than that in the bulk.

In both cases, the insets show the normalized $\Delta P(T)/P_0(T)$ ratios. An increase in the $\Delta P(T)/P_0(T)$ ratio following a decrease in the temperature (see Fig. 4, *b*, inset) shows that the saturation vapor pressure decreases with increase in temperature much faster than does the width of the loop on the descending branch. A similar dependence of the hysteresis width on temperature is shown in Fig. 4, *c*.

It is noteworthy that the full temperature range covers the liquid—solid phase transitions; therefore, for capillary condensation the region of very low temperatures has no physical meaning. In the real range of temperature measurements ($\tau \geq 0.5$), the hysteresis loop width increases with a decrease in temperature. Below we use normalized $\Delta P/P_0$ ratios at a specified temperature, as they are directly observed in experiments.

Effect of the molecular properties of the system on the hysteresis loop. As noted above, the width of the adsorption hysteresis loop is affected by all molecular properties of the adsorbent—adsorbate system. The effect of the nature of the pore wall surface, which is specified by the adsorbent—adsorbate energy value, on the equilibrium pressure and the normalized width of the hysteresis loop in slit-shaped ($H = 10\delta$) and cylindrical ($D = 15\delta$) pores is illustrated in Fig. 5. In cylindrical pores, the calculation was carried out with a wall potential 2 (*3*) or 3 (*4*) monolayers long ($z = 12$). The greater the length of the wall potential, the smaller the central region of the pore with $Q_f = 0$ in which the capillary condensation of the adsorbate takes place and the narrower the hysteresis loop.

The nature of the pore wall surface has relatively little influence on the hysteresis width for slit-shaped and cylindrical pores in the region of relatively strong adsorbate—adsorbent interaction, more precisely, when the dimensionless ratio $\alpha = Q_1/\varepsilon > 3$ ($z = 12$) and $Q_1/\varepsilon > 2$ ($z = 6$). For attracting walls, the pressure P_0 decreases with respect to the P_0 value for the bulk phase, the pore size being invariable (see Fig. 5, *a*). Similarly, the width of the hysteresis loop remains almost the same (see Fig. 5, *b*).

When $Q_1/\varepsilon < 3$ for $z = 12$ and $Q_1/\varepsilon < 2$ for $z = 6$, the saturation vapor pressure (see Fig. 5, *a*) approaches or exceeds the P_0 value. This energy range will be conventionally denoted as corresponding to "weak adsorption". The equality $P_0(H,D) = P_0$ holds for $Q_1/\varepsilon \approx 0.6$—$1.5$ for slit-shaped and cylindrical pores. The ratio $P_0(H,D) > P_0$ for $Q_1/\varepsilon < 0.6$—1.5 corresponds to poorly wettable walls (or non-wettable at $Q_1/\varepsilon \approx 0$), while the opposite relationship $P_0(H,D) < P_0$ at $Q_1/\varepsilon > 0.6$—1.5 refers to wettable pore walls. For weak adsorption, the loop width sharply increases with a decrease in the adsorbent—adsorbate bond energy (see Fig. 5, *b*).

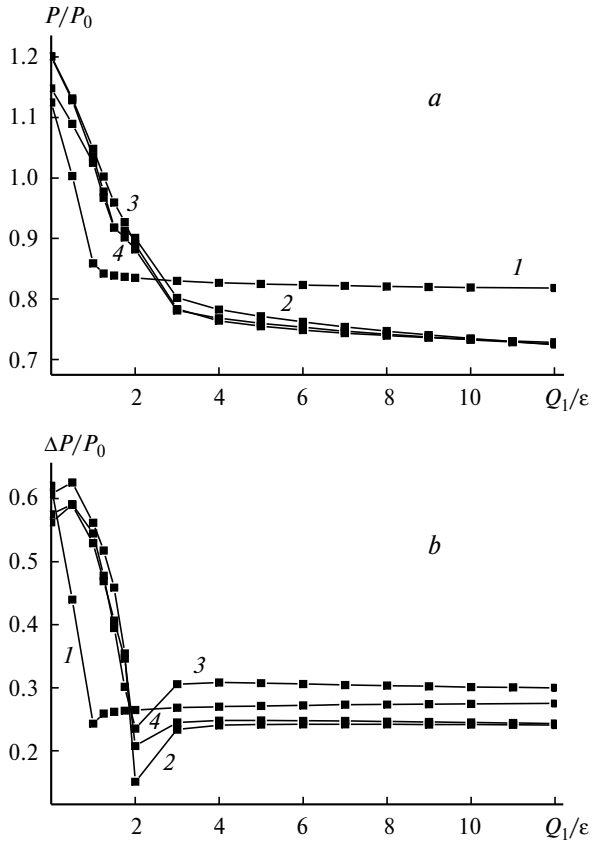

Fig. 5. Saturation vapor pressure P/P_0 (*a*) and normalized width of the hysteresis loop $\Delta P/P_0$ (*b*) *vs.* adsorbent—adsorbate interaction energy for slit-shaped pores of width $H = 10\delta$, $z = 6$ (*1*) and 12 (*2*) and cylindrical pores with the diameter $D = 15\delta$, $z = 12$ (*3*, *4*). The calculations for the cylindrical pore differ by the length of the wall potential: 2 (*3*) and 3 (*4*) monolayers.

It should be emphasized that a decrease or increase in the saturation vapor pressure in a pore is determined by molecular parameters of the adsorbent—adsorbate system and is not related explicitly to the meniscus curvature at the vapor—liquid interface inside the pore (as is usually suggested when the Kelvin equation is used). An implicit relationship between the bond energy and the meniscus curvature does obviously exist. Also, for both types of pores at $Q_1/\varepsilon > 3.0$, all materials can be considered conventionally to be equally highly wettable. The results (see Fig. 5) demonstrate that the type of adsorption influences the saturation vapor pressure inside the pores and the width of the hysteresis loop.

An analogous difference between the equilibrium phase diagrams for weak and strong adsorption has been noted

previously.[24] To this end, the dimensionless parameter $\gamma = \varepsilon_{As}/\varepsilon_{AA}$ determined from the Lennard-Jones parameters of potential curves was introduced. All range of γ values was split conventionally into two parts: $\gamma < 0.2$ ("weak" adsorption) and $\gamma > 0.4$ ("strong" adsorption). The phase diagrams for these cases are qualitatively different for slit-shaped pores of small sizes,[24] in particular, the critical temperature varies non-monotonically (monotonically) as a function of the pore width for strong (weak) adsorption. In the intermediate range $0.2 < \gamma < 0.4$, the form of the phase diagram cannot be reliably predicted based on the parameters of potential curves alone, and a numerical analysis of the total energies of the interaction of adsorbate molecules with the wall and with one another is required. (The use of the ratio of the total energy Q_1 to ε is more vivid than the ratio of the parameters ε_{ij}.)

The effect of the pore size factor is illustrated by Fig. 6. Figures 6, *a* and *b* show the dependences of the saturation vapor pressure $P_0(H,D)$ and the width of the hysteresis loop on the characteristic pore size (Ar—SiO_2 system) for the same molecular parameters as in Fig. 5. The pore geometry and characteristic size play an important role in

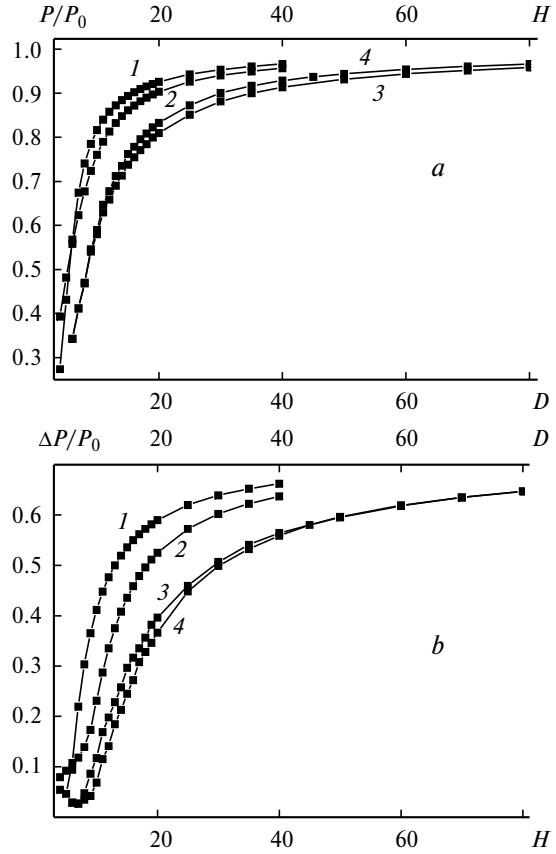

Fig. 6. Saturation vapor pressure (*a*) and width of the hysteresis loop (*b*) *vs.* characteristic pore size (Ar—SiO_2 type systems) for slit-shaped (*1*, *2*) and cylindrical (*3*, *4*) pores. For parameters, see the caption to Fig. 5.

determining the saturation vapor pressure inside the pore. The type of pore cross-section has a much more pronounced effect than the change in the lattice structure z or the length of the surface potential of the wall (see Fig. 6, *a*). As the pore width increases, the pressure in the slit reaches the bulk pressure more rapidly than in the case of cylindrical pore.

The value $H = 6\delta$ is the first value that makes possible the presence of the loop in the central part of the pore (*i.e.*, capillary condensation), because for $H = 5\delta$, the critical temperature of the central dome is approximately equal to the critical temperature of near-surface domes.[24] In addition, $\Delta P/P_0 \geq 0.55$ can be regarded as the lower limit of the observable loops corresponding to central regions. For $H < 6\delta$, a hysteresis loop is also possible but only for adsorption in microporous adsorbents.[2] For $H/\delta = 6—10$, an influence of an evenness or oddness of the pore width on the adsorbate critical density is observed[24] (as H is further increased, this factor is no longer significant), and the hysteresis width sharply decreases in this region of H values (see Fig. 6, *b*).

For cylindrical pores, the loop width decreases more rapidly. When $D = 6\delta$, one gets $\Delta P/P_0 \approx 0$. This means that for a 2-nm region, the hysteresis is virtually missing and has a clear-cut shape only at $\Delta P/P_0 > 0.1$, which corresponds to cylinders with a diameter of more than 3 nm. In order to carry out quantitative comparison of the numerical data with nitrogen and argon adsorption experiments in mesoporous materials of the MCM-41 type,[31,32] it is necessary to take into account the calibration function[33] the influence of which is not considered in this communication.

Effect of the pore wall heterogeneity on the conditions of capillary condensation is illustrated by Fig. 7. The degree of heterogeneity of the cylindrical pore walls was varied for two diameters of the MCM-41 samples.[31,32] Four variants of calculation of the adsorption isotherms with adsorption spinodal branches are presented (four numbers of the curves). The calculated curves at a temperature of 87.3 K ($\tau = 0.58$) differ in the degree of amorphization of the surface material. The homogeneous pore walls (without amorphization) are shown by curves *1* and *2*. The energy parameters of heterogeneous walls for curves *5* and *6* were obtained previously[34] from experimental data on argon adsorption on a flat silica gel surface (see Ref. 2, p. 84) taking into account the effect of wall curvature in different cylindrical channels. The parameters of curves *3* and *4* correspond to a twofold decrease in the degree of amorphization, while parameters of curves *7* and *8* were obtained with a twofold increase in the degree of amorphization with respect to those of curves *5* and *6*.

The resulting curves demonstrate that, although capillary condensation takes place in the central part of the pore, the variation of the properties of pore walls has an influence on the position and the width of the adsorp-

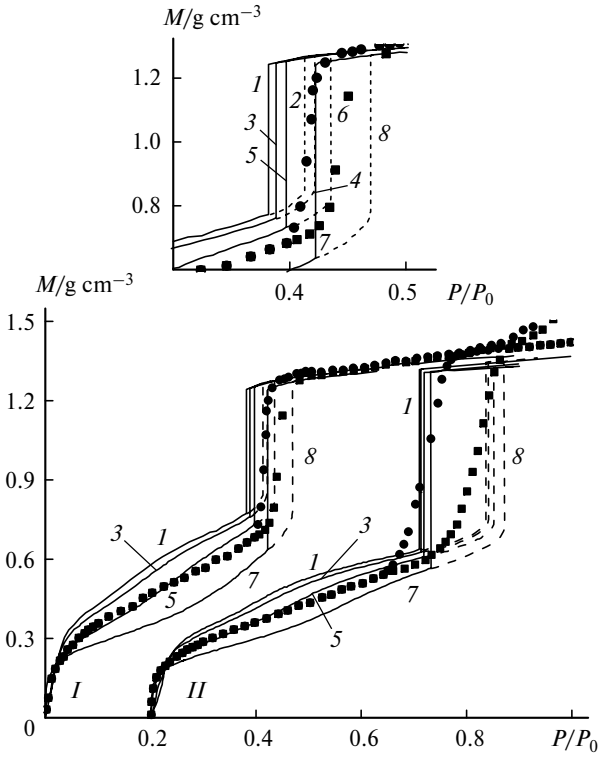

Fig. 7. Argon adsorption and desorption isotherms as functions of the ihnomogeneity of cylindrical pore walls of MCM-41 with diameters of 4.15 nm (*I*)[31] and 5.54 nm (*II*)[32]. The odd numbers of the curves correspond to desorption branches and the even numbers correspond to adsorption branches. Curves *1*, *2* refer to homogeneous walls; for curves *5*, *6*, wall heterogeneity corresponds to the experiment;[35] for the pairs of curves *3*, *4* and *7*, *8*, the adsorbate—adsorbent interaction energy is half that and twice that for curves *5*, *6*, respectively. The family of curves *II* is shifted by 0.2 along the pressure axis. The "circle" and "square" characters correspond to the desorption and adsorption branches of both experimental isotherms, respectively. The inset shows isotherms *I* on a larger scale.

tion—desorption hysteresis loop. For these variations of the pore wall properties, the $\Delta P/P_0$ values vary from 0.031 to 0.046 for a 4.4 nm pore and from 0.127 to 0.138 for a 5.4 nm pore.

These calculations show that the considered model reflects qualitatively the experimental data for both the region of existence and the width of the hysteresis loop. A quantitative description requires that the polydispersity of MCM-41 be taken into account: the experimental hysteresis branches vary monotonically with increase in pressure, whereas theoretical calculations for monodisperse systems predict density jumps on the hysteresis branches.

* * *

Full spinodal diagrams for narrow-pore systems were constructed for the first time. It was shown that the type of the density—temperature diagrams for the gas and liquid spinodal branches in the pores is similar to the type of equilibrium vapor—liquid phase diagrams: they have a common critical point and the branches for the dense phase are shifted to lower densities, while the branches for the rarefied phase are shifted to higher densities. The spinodal diagrams for narrow-pore systems, like the phase diagrams, have multidome structures.

It was shown that the width of the adsorption—desorption hysteresis loop depends on all the molecular properties of the adsorbate—adsorbent system. The hysteresis loop width is also affected by the temperature of measurement. Therefore, when solving the problem of increasing the accuracy of determination of the pore size distribution function from the experimental adsorption isotherms having a hysteresis, one should take into account both the specific features of the mesoporous adsorbent—adsorbate system under study and the experimental conditions.

The results reported in the communication attest to a complex nature of the capillary condensation processes in narrow pores. Figures 1, *b*, 2, *b* and calculations[24] indicate that the condensation occurs in slit-shaped pores seven monolayers wide, whereas for activated carbons with the same characteristic size (~2 nm), no density jump is observed in the experiment.[1—5] This is due to the difference between the model that implies an infinite length of the pore along two directions and the real limited pore regions in microporous systems. This issue will be discussed in detail in the next communication.[35] Meanwhile, the model calculations for the temperature dependences of the width of the hysteresis loop (see Fig. 4) that pass through a maximum coincide qualitatively with the results of experimental studies of the capillary condensation phenomena over broad temperature and pressure ranges.[36]

The calculations were carried out for strictly monodisperse porous systems. In the first approximation, mesoporous materials MCM-41 can be classified as systems of this type.[31,32] These are characterized by some scatter of cylindrical pores according to diameters but the pores themselves have greater lengths across the adsorbent. Transitions between pores of different size are almost missing; therefore, the MCM-41 materials show no mutual blocking effects for pores of different size in the adsorption and desorption processes, which are usually considered to be responsible for differences in the pore size distribution functions estimated from the adsorption and desorption isotherm branches.[1—3] Study of polydispersed porous systems by this approach would help to elucidate the role of these blockings and interpret the differences in the pore size distribution functions estimated from different branches of isotherms.

This work was financially supported by the Russian Foundation for Basic Research (Project No. 06-03-32031a).

References

1. D. H. Everett, in *The Solid—Gas Interface*, Ed. E. A. Hood, Dekker, New York, 1967, 1055 p.
2. S. J. Gregg and K. G. W. Sing, *Adsorption, Surface Area, and Porosity*, Acad. Press, London, 1982.
3. T. G. Plachenov and S. D. Kolosentsev, *Porometriya* [*Porometry*], Khimiya, Leningrad, 1988, 175 pp. (in Russian).
4. A. P. Karnaukhov, *Adsorptsiya. Tekstura dispersnykh poristykh materialov* [*Adsorption. Texture of Dispersed Porous Materials*], Nauka, IK SO RAN, Novosibirk, 1999, 469 pp. (in Russian).
5. *Eksperimental´nye metody v adsorptsii i moleculeyarnoi khromatografii* [*Eksperimental Methods in Adsorption and Molecular Chromatography*], Eds. A. V. Kiselev and V. P. Dreving, Izd. MGU, Moscow, 1973, 447 pp. (in Russian).
6. R. Evans, *J. Phys.: Condens. Matter.*, 1990, **46**, 8989.
7. V. P. Skripov and M. Z. Faizullin, *Fazovye perekhody kristall—zhidkost´—par i termodinamicheskoe podobie* [*Phase Transitions Crystal—Liquid—Vapor and Thermodynamic Similarity*], Fizmatlit, Moscow, 2003, 160 pp. (in Russian).
8. M. W. Maddox, J. P. Olivier, and K. E. Gubbins, *Langmuir*, 1997, **13**, 1737.
9. P. I. Ravikovitch, S. C. O´Domhnaiu, A. V. Neimark, F. Schiith, and K. K. Unger, *Langmuir*, 1995, **11**, 4765.
10. R. Evans, U. M. B. Marconi, and P. Tarazona, *J. Chem. Phys.*, 1986, **84**, 2376.
11. K. Binder and D. P. Landau, *J. Chem. Phys.*, 1992, **96**, 1444.
12. E. V. Votyakov, Yu. K. Tovbin, J. M. D. MacElroy, and A. Roche, *Langmuir*, 1999, **15**, 5713.
13. Yu. K. Tovbin and T. V. Petrova, *Zh. Fiz. Khim.*, 1995, **69**, 127 [*Russ. J. Phys. Chem.*, 1995, **69** (Engl. Transl.)].
14. A. V. Neimark, P. I. Ravikovitch, and A. Vishnyakov, *Phys. Rev. E*, 2000, **62**, 2.
15. Yu. K. Tovbin, *Teoriya fiziko-khimicheskikh protsesov na granitse gaz—tverdoe telo* [*Theory of Physocochemical Processes at the Gas—Solid Interface*], Nauka, Moscow, 1990, 288 p. (in Russian).
16. Yu. K. Tovbin, *Izv. Akad. Nauk. Ser. Khim.*, 2003, 827 [*Russ. Chem. Rev., Int. Ed.*, 2003, **52**, 869].
17. Yu. K. Tovbin and D. V. Eremich, *Izv. Akad. Nauk. Ser. Khim.*, 2003, 2208 [*Russ. Chem. Rev., Int. Ed.*, 2003, **52**, 2334].
18. Yu. K. Tovbin and D. V. Yeremich, *Colloids and Surfaces A*, 2002, **206**, 363.
19. Yu. K. Tovbin and D. V. Eremich, *Zh. Fiz. Khim.*, 2004, **78**, 720 [*Russ. J. Phys. Chem.*, 2004, **78** (Engl. Transl.)].
20. A. M. Vishnyakov, E. M. Piotrovskaya, E. N. Brodskaya, E. V. Votyakov, and Yu. K. Tovbin, *Zh. Fiz. Khim.*, 2000, **74**, 501 [*Russ. J. Phys. Chem.*, 2000, **74**, 3].
21. E. V. Votyakov, Yu. K. Tovbin, J. M. D. MacElroy, and A. Roche, *Langmuir*, 1999, **15**, 5713.
22. W. A. Steele, *The Interactions of Gases with Solid Surfaces*, Pergamon, New York, 1974.
23. Yu. K. Tovbin and E. V. Votyakov, *Zh. Fiz. Khim.*, 1998, **72**, 1885 [*Russ. J. Phys. Chem.*, 1998, **72** (Engl. Transl.)].
24. Yu. K. Tovbin and E. V. Votyakov, *Izv. Akad. Nauk. Ser. Khim.*, 2001, 48 [*Russ. Chem. Rev., Int. Ed.*, 2001, **50**, No. 1].
25. M. E. Fisher and H. Nakanishi, *J. Chem. Phys.*, 1981, **75**, 5857.
26. H. Nakanishi and M. E. Fisher, *J. Chem. Phys.*, 1983, **78**, 3279.
27. P. Tarasona, U. M. B. Marconi, and R. Evans, *Mol. Phys.*, 1987, **60**, 573.
28. A. de Kreizer, T. Michalski, and G. H. Findenegg, *Pure Appl. Chem.*, 1991, **63**, 1495.
29. Yu. K. Tovbin and E. V. Votyakov, *Langmuir*, 1993, **9**, 2652.
30. E. V. Votyakov and Yu. K. Tovbin, *Zh. Fiz. Khim.*, 1994, **68**, 287 [*Russ. J. Phys. Chem.*, 1994, **68** (Engl. Transl.)].
31. P. I. Ravikovitch, D. Wei, W. T. Chueh, G. L. Haller, and A. V. Neimark, *J. Phys. Chem.*, 1997, **101**, 3671.
32. M. Kruk and M. Jaroniec, *Chem. Mater.*, 2000, **12**, 222.
33. Yu. K. Tovbin, A. B. Rabinovich, and E. V. Votyakov, *Izv. Akad. Nauk. Ser. Khim.*, 2002, 1531 [*Russ. Chem. Rev., Int. Ed.*, 2002, **51**, 1667].
34. Yu. K. Tovbin and A. G. Petukhov, *Zh. Fiz. Khim.*, 2007, **81**, № 9 [*Russ. J. Phys. Chem.*, 2007, **81**, No. 9 (Engl. Transl.)].
35. Yu. K. Tovbin and A. G. Petukhov, *Izv. Akad. Nauk. Ser. Khim.*, 2007, No. 8 [*Russ. Chem. Bull., Int. Ed.*, 2007, **56**, No. 8].
36. Nguen-thi Min Hien and V. V. Serpinskii, *Izv. Akad. Nauk SSSR. Ser. Khim.*, 1987, 2421 [*Bull. Acad. Sci. USSR, Div. Chem. Sci.*, 1987, **36** (Engl. Transl.)].

Received December 28, 2006;
in revised form April 23, 2007